



Cite this: *Phys. Chem. Chem. Phys.*,  
2025, 27, 23022

## Rotational excitation of fulminic acid (HCNO) in collisions with molecular hydrogen

Paul J. Dagdigian 

Integral cross sections and rate coefficients for the rotational excitation of fulminic acid (HCNO) induced by collisions with molecular hydrogen are reported in this work. These quantities were derived through quantum time independent close coupling calculations. These calculations employed a potential energy surface (PES) computed using the explicitly correlated coupled cluster method that included single, double, and (perturbatively) triple excitations [CCSD(T)-f12a] and a correlation consistent aug-cc-pVTZ basis. The geometries of the molecular partners were assumed to be fixed. The global minimum of the PES was found to have an energy of  $-289.1\text{ cm}^{-1}$  relative to the energy of the separated molecules, and the equilibrium intermolecular separation equals  $5.64a_0$ . The computed points of the PES were fit to a form suitable for time-independent quantum scattering calculations. Calculated HCNO-H<sub>2</sub> rate coefficients were compared with scaled previously calculated HCNO-He rate coefficients. A simple radiative transfer model was applied to HNCO and HCNO lines; the ratio of the intensities of these lines was found to vary strongly for H<sub>2</sub> volume densities between  $10^4$  and  $10^6\text{ cm}^{-3}$ .

Received 29th August 2025,  
Accepted 14th October 2025

DOI: 10.1039/d5cp03326h

rsc.li/pccp

### 1 Introduction

Isocyanic acid (HNCO) was one of the first molecules detected by radioastronomy; Snyder and Buhl<sup>1</sup> detected this molecule toward Sgr B2. HNCO has been found in high abundance toward molecular clouds in the direction of the galactic center<sup>2–4</sup> and has been observed in other environments such as hot molecular cores,<sup>5–8</sup> molecular outflows,<sup>9</sup> external galaxies,<sup>10–12</sup> and comets.<sup>13,14</sup>

HNCO is the simplest molecule containing one atom each of the important elements H, C, N, and O and is the most stable isomer with this empirical formula. In addition, there are three isomers of HNCO, in order of decreasing stability: cyanic acid (HOCN), fulminic acid (HCNO), and isofulminic acid (HONC).

Brünken *et al.*<sup>15</sup> recorded the rotational microwave spectrum and also reported tentative detection of HOCH in Sgr B2(OH) in the interstellar medium. They estimated an approximate HOCH column density of  $6 \times 10^{12}\text{ cm}^{-2}$ , or approximately 0.5% of the column density of the more abundant HNCO molecule. In a further investigation, HOCH was detected in a quiescent molecular cloud in the Galactic center. In an additional investigation, a fairly constant HOCH abundance ratio of 0.3–0.8% relative to HNCO over the extended gas components was observed.<sup>16</sup>

Marcelino *et al.*<sup>17</sup> reported the first astronomical detection of the HCNO isomer in three starless cores and in the low-mass

star-forming region L1527. Carnicharo *et al.*<sup>18</sup> detected the isotopolog DCNO in TMC-1 and determined an HCNO/DCNO ratio of  $25 \pm 4$ . The microwave rotational spectrum of HCNO, and its deuterated isotologue DCNO, was first reported by Bodenseh and Winniwyser.<sup>19</sup> To shed some light on possible formation pathways for these isomers, in a subsequent study Marcelino *et al.*<sup>20</sup> searched for HOCH in regions where HCNO had been previously detected. HOCH was detected in three dense cores and the lukewarm corino where HCNO had been detected. By contrast, HOCH was detected toward the protostellar binary IRAS 16293-2422; however, HCNO was not detected in this source, nor in sources where HOCH had been previously reported. The rotational microwave spectrum of the least stable isomer of HNCO, namely isofulminic acid (HONC) was been reported,<sup>21</sup> but this detection of this molecule in the interstellar medium has not been reported.

It is of great interest to estimate molecular column densities from the measured intensities of the microwave rotational transitions. This can be most straightforwardly carried out if local thermodynamic equilibrium (LTE) can be assumed. However, the total molecular density in most interstellar clouds is orders of magnitude lower than that for LTE to apply. Under these conditions, the estimation of molecular abundance from measured spectroscopic intensities requires application of a radiative transfer model, for example that described by van der Tak *et al.*<sup>22</sup> Population is transferred between rotational levels by collisions with the dominant interstellar species, usually H<sub>2</sub>. In addition, decay of the populations of excited rotational levels also occurs through spontaneous radiative transitions, the rates

Department of Chemistry, The Johns Hopkins University, Baltimore, MD 21218, USA. E-mail: [pjdagdigian@jhu.edu](mailto:pjdagdigian@jhu.edu)



of which are typically available, for example, from the Cologne Database for Molecular Spectroscopy (CDMS).<sup>23</sup> The rate coefficients for transfer between molecular rotational levels induced by collisions with H<sub>2</sub> must be calculated for each collision pair. Such calculations require a two-step process, in which the potential energy surface (PES) must first be computed for the collision pair of interest and then the rate coefficients for collision transfer must be calculated usually through quantum scattering calculations.

Rate coefficients have been reported for several collision pairs involving HNCO and its isomers. Sahnoun *et al.*<sup>24</sup> have reported rate coefficients for collisions of HNCO with H<sub>2</sub>, using a CCSD(T)-f12a HNCO–H<sub>2</sub> PES which they computed. Helium is often employed as a surrogate for H<sub>2</sub> to compute rate coefficients more simply. With scaling by the collision reduced mass, these rate coefficients are then used as substitutes to describe the rate coefficients appropriate for collisions with H<sub>2</sub>. Naindouba *et al.*<sup>25</sup> have computed a PES for the interaction of HCNO with He and used this surface to compute rate coefficients for HCNO–He collisions. It will be interesting to compare the HCNO–H<sub>2</sub> rate coefficients described in this work with scaled HCNO–He rate coefficients. Finally, Naouai and Jrad<sup>26</sup> have reported rate coefficients for HOCH<sub>2</sub>–He collisions, based on a PES calculated in that work.

In this work, time independent quantum scattering calculations are employed to determine cross sections and rate coefficients for transitions induced in HCNO through collisions with H<sub>2</sub>. Here, the scattering wave function, which is expanded over a basis of internal levels of the complex, is integrated from the classically forbidden small-*R* region to an asymptotically large *R*. The *S*-matrix, and then the cross sections, are obtained from the large-*R* wave function. Several other approaches have been employed in other studies to determine the collision cross sections. For example, quantum dynamical time-dependent wavepacket theory has been applied to triatomic and tetraatomic systems, mainly in reactive collisions.<sup>27–29</sup> For nonreactive collisions, the mixed quantum classical theory<sup>30</sup> and the statistical adiabatic model<sup>31</sup> show great promise for large systems.

The remainder of this paper is organized in the following manner. Section 2 presents a description of the quantum chemistry calculations of points on the HCNO–H<sub>2</sub> PES and describes a fit of the calculated points to a functional form appropriate for time independent quantum scattering calculations. A brief description of properties of the PES is also presented in this section. Section 3 describes the formalism and details of the scattering calculations. The computed cross sections and rate coefficients are reported and discussed in Section 4. The paper concludes with a discussion section (Section 5).

## 2 Potential energy surface

The equilibrium structure of fulminic acid is known to be linear.<sup>32</sup> This molecule is floppy, with a low frequency of the bending vibrational mode (224 cm<sup>-1</sup>).<sup>33</sup> The energies of the rotational levels of the ground vibrational level are well

Table 1 Body-frame coordinates (in  $a_0$ ) of the atoms in HCNO

Atom	<i>x</i>	<i>y</i>	<i>z</i>
H	0	0	2.2827
C	0	0	1.2307
N	0	0	0.0717
O	0	0	-1.1303

described by the standard rotational energy form, with rotational constants  $B = 0.382566$  cm<sup>-1</sup> and  $D = 1.4216 \times 10^{-7}$  cm<sup>-1</sup>. In view of this rotational structure, we will take the molecule as rigid and linear for the purpose of computing a potential energy surface.

Bodenseh and Winnewisser<sup>19</sup> have determined the bond lengths from the measured rotational constants of the ground vibrational levels of HCNO and DCNO, and we use their bond lengths in this work. We place the HCNO molecule in the body-frame coordinate system along the *z* axis with the HCNO center of mass fixed at the origin of the coordinate system. In our calculation of the PES for HCNO–H<sub>2</sub>, we have assumed a rigid linear HCNO structure. The Cartesian coordinates of the atoms in HCNO are given in Table 1. It can be seen in this table that the H atom is considerably displaced from the center of mass. We can anticipate that the PES is very anisotropic.

### 2.1 Quantum chemistry calculations

The HCNO molecule is positioned so that the H end of the molecule points toward the positive *z* direction. The separation of the centers of mass of the HCNO and H<sub>2</sub> molecules is denoted *R*. The Jacobi **R** vector is placed in the body-frame *xz* plane, and  $\theta_1$  denotes the angle between the *z* axis and **R**. The angle between the H<sub>2</sub> bond axis and the *z* axis is denoted  $\theta_2$ . The dihedral angle  $\phi$  denotes the angle between the body-frame *x* axis and the projection of the H<sub>2</sub> bond axis on the *xy* plane.

The PES describing the interaction between HCNO and H<sub>2</sub> molecules was calculated using the MOLPRO suite of programs.<sup>34</sup> Here, explicitly correlated coupled cluster theory with inclusion of single, double, and (perturbatively) triple excitations [CCSD(T)-f12a] was utilized.<sup>35</sup> The aug-cc-pVTZ basis was employed in the calculations,<sup>36,37</sup> with VTZ/MP2FIT,<sup>38</sup> and the density fitting basis and resolution of the identity.<sup>39</sup> A counterpoise correction was applied to correct for basis set superposition error.<sup>40</sup>

Some test calculations were carried out to check the convergence of the calculations with respect to the size of the basis set. Fig. 1 presents radial cuts with the aug-cc-pVTZ and aug-cc-pVQZ basis sets at the orientation of the absolute minimum of the PES. It can be observed that the well depth  $D_e$  computed with the aug-cc-pVQZ basis set is 289.1 cm<sup>-1</sup>, or 1.0 cm<sup>-1</sup> greater than the well depth computed with the aug-cc-pVTZ basis set. The equilibrium intermolecular separation, calculated using the aug-cc-pVQZ basis set was found to equal 5.64  $a_0$ . The difference in the computed well depth is sufficiently small that calculation of the PES with the aug-cc-pVTZ basis set should be sufficiently accurate here. Calculation with the larger basis set would require an inordinately greater calculation time.

The HCNO–H<sub>2</sub> interaction energy was calculated on a 4-dimensional grid (*R*,  $\theta_1$ ,  $\theta_2$ ,  $\phi$ ) consisting of 30 values of the

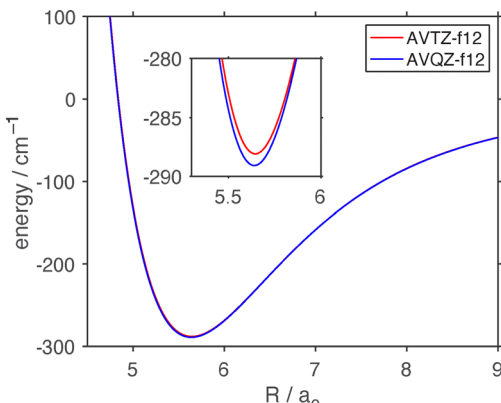


Fig. 1 Radial cuts of the HCNH–H<sub>2</sub> potential energy surface for an orientation near to that of the global minimum ( $\theta_1 = 102^\circ$ ,  $\theta_2 = 48^\circ$ ,  $\phi = 0^\circ$ ).

intermolecular separation  $R$  ranging from  $3.5$  to  $20a_0$ . The angles defining the orientation of the complex were chosen randomly in order to sample the PES in an unbiased manner.<sup>41</sup> Calculations were performed at  $2000$  random orientations for each value of  $R$ .

## 2.2 Fitting the potential energy surface

The biharmonic expansion derived by Green,<sup>42</sup> appropriate to describe the interaction of two linear molecules, was employed to fit the calculated points on the HCNO–H<sub>2</sub> PES. The form of this expansion can be written as

$$V(R, \theta_1, \theta_2, \phi) = \sum_{l_1 l_2 l} v_{l_1 l_2 l}(R) \bar{t}_{l_1 l_2 l}(\theta_1, \theta_2, \phi) \quad (1)$$

where

$$\bar{t}_{l_1 l_2 l}(\theta_1, \theta_2, \phi) = [(2l + 1)/4\pi]^{1/2} (l_1 m l_2, -m | l_0) Y_{l_1 m}(\theta_1, \phi) Y_{l_2, -m}(\theta_2, \phi) \quad (2)$$

and  $(\dots | \dots)$  is a Clebsch–Gordan coefficient and  $Y_{lm}$  is a spherical harmonic.<sup>43</sup>

The non-negative integer indices  $l_1$ ,  $l_2$ , and  $l$  define the tensor ranks of the angular dependence of the HCNO orientation, the H<sub>2</sub> orientation and the collision vector orientation, respectively. The allowed values of  $l$  are set by the vector addition of  $l_1$  and  $l_2$ . Only even values of  $l_2$  are allowed because of the homonuclear character of H<sub>2</sub>. The sum  $l_1 + l_2 + l$  must be an even integer since the potential should be parity invariant, *i.e.* unchanged in inversion of all coordinates through the origin.<sup>44</sup>

The PES is extremely repulsive for certain orientations of HCNO and H<sub>2</sub>O for smaller values of  $R$ . Since these repulsive regions are not sampled in the scattering calculations, the potential was damped in these regions with a hyperbolic tangent function up to a maximum value  $V_{\max}$ .<sup>45</sup> The damped potential  $\bar{V}$  is unchanged from the original potential  $V$  for values less than  $V_0$ . Specifically, the damped potential is given by

$$\begin{aligned} \bar{V} &= V & \text{for } V \leq V_0 \\ &= V_0 + \beta^{-1} \tanh[\beta(V - V_0)] & \text{for } V > V_0 \end{aligned} \quad (3)$$

Table 2 Fits of points on the HCNO–H<sub>2</sub> PES at  $R = 6.5a_0$

$l_1^{\max}$	$l_2^{\max}$	No. of coefficients	Std. dev. (cm <sup>-1</sup> )
20	4	176	0.2608
22	4	194	0.2360
24	4	212	0.1749
26	4	230	0.1075
28	4	248	0.0841
30	4	266	0.0777
32	4	284	0.0602
34	4	302	0.0476
36	4	320	0.0461

where  $\beta = [V_{\max} - V_0]^{-1}$ . In this work,  $V_0$  was set to  $2000$  cm<sup>-1</sup> and  $V_{\max} = 2V_0$ . With this damping function, contour plots of the PES were found to vary smoothly as a function of the orientation.

The expansion coefficients describing the PES, defined in eqn (1) and (2) were determined for each  $R$  by a least squares fit of the interaction energies computed at the  $2000$  random orientations. Fits were performed with different numbers of coefficients, determined by the maximum values  $l_1^{\max}$  and  $l_2^{\max}$  of the terms included the sum in eqn (1).

To determine the optimum set of coefficients to describe the PES, fits were carried out with different values of  $l_1^{\max}$  and  $l_2^{\max}$  for  $R = 6.5a_0$ , in the attractive region of the PES. The results of these fits are presented in Table 2. It can be seen in Table 2 that the standard deviation of the fit reaches an asymptotic value (*ca.*  $0.046$  cm<sup>-1</sup>) only at  $l_1^{\max} = 34$ . As Table 2 shows, the use of expansion coefficients of the PES determined with  $l_1^{\max} = 36$ ,  $l_2^{\max} = 4$  requires  $320$  coefficients to describe the PES. This is a large number of coefficients to carry in the scattering calculations.

To explore whether a smaller number of coefficients can be employed to describe the PES, contour plots computed with fitted coefficients determined with different values of  $l_1^{\max}$  were compared. Fig. 2 compares contour plots for  $R = 6.5a_0$  computed with angular coefficients determined by least squares fits with  $l_1^{\max} = 36$  and  $28$ ,  $l_2^{\max} = 4$ . To within the resolution of the figure, these two contour plots are indistinguishable. The fit obtained with  $l_1^{\max} = 28$ ,  $l_2^{\max} = 4$  (248 coefficients) was deemed as acceptable for use in the scattering calculations. It was not possible to reduce the number of coefficients by selectively eliminating some terms, as this author has done in previous work,<sup>46–48</sup> and maintain the integrity of the contour plots.

The set of  $248$  angular coefficients for all intermolecular separations in the radial grid were computed by least squares fits with  $l_1^{\max} = 28$ ,  $l_2^{\max} = 4$ . The coefficients that have significant magnitude at the largest  $R$  in the radial grid were extended with a hyperbolic tangent function to a  $R^{-n}$  dependence at large  $R$ . In particular, the isotropic term ( $l_1 = 0$ ,  $l_2 = 0$ ,  $l = 0$ ) was extended with a  $R^{-6}$  dependence at large  $R$ . Terms which involve a multipole–multipole interaction, for example, dipole–quadrupole and quadrupole–quadrupole interactions, were extended with an appropriate  $R^{-n}$  dependence. Other terms were damped to zero at large  $R$  using the hyperbolic tangent function.

The well depth  $D_e$  of the PES, calculated with the aug-cc-pVQZ basis set, was found to equal  $289.1$  cm<sup>-1</sup>. The equilibrium



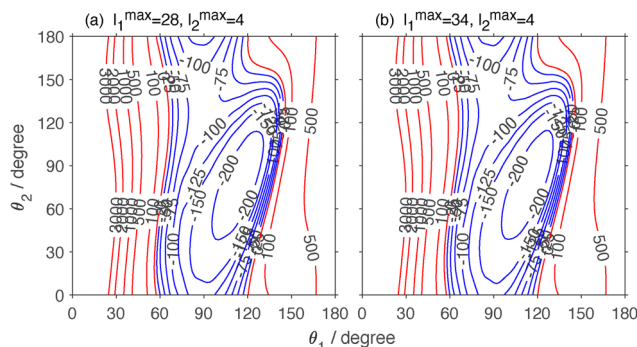


Fig. 2 Contour plots of the HCNO–H<sub>2</sub> potential energy surface at  $R = 6.5a_0$  for variation of the polar angles  $\theta_1$  and  $\theta_2$  for fixed dihedral angle  $\phi = 0^\circ$ . The potential energy was calculated with (a) the 248 angular expansion coefficients determined with  $l_1^{\max} = 18$  and  $l_2^{\max} = 4$  and (b) the 302 angular expansion coefficients determined with  $l_1^{\max} = 34$  and  $l_2^{\max} = 4$ .

intermolecular separation was determined to be  $5.64a_0$ . The angles defining the global minimum equal  $\theta_1 = 102^\circ$ ,  $\theta_2 = 48^\circ$ ,  $\phi = 0^\circ$ , and the geometry at the global minimum of the PES is illustrated in Fig. 3. The H<sub>2</sub> molecule is located on the side of the HCNO molecule, nearly perpendicular to the HCNO bond axis. No secondary minima were found on the PES.

### 3 Cross sections and rate coefficients

The Hibridon suite of programs<sup>49</sup> was employed for the calculation of cross sections of rotationally inelastic transitions induced in HCNO by collisions with molecular hydrogen, namely.



The rotational levels of HCNO and H<sub>2</sub> are denoted  $j_1$  and  $j_2$ , respectively. The formalism describing collisions of two linear molecules was derived by Green.<sup>42</sup>

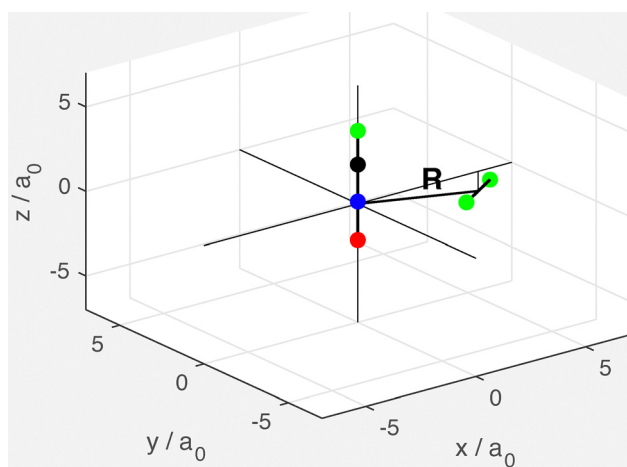


Fig. 3 Geometry of the global minimum of the HCNO–H<sub>2</sub> complex. The Jacobi vector is indicated in the figure. The equilibrium intermolecular separation  $R$  equals  $5.64a_0$ , and the angles defining the orientation of the complex are  $\theta_1 = 102^\circ$ ,  $\theta_2 = 48^\circ$ ,  $\phi = 0^\circ$ . The color coding of the atoms is as follows: H, green; C, black; N, blue; O, red.

The energies of the HCNO rotational levels were taken from the CDMS database.<sup>23</sup> Since *para*-H<sub>2</sub> (only  $j_2 = 0$  here) and *ortho*-H<sub>2</sub> (only  $j_2 = 1$  here) are not interconverted by gas-phase molecular collisions, separate calculations were carried out for the two nuclear spin modifications. The Hibridon suite of programs<sup>49</sup> was employed for this purpose. In what follows, we write *p*-H<sub>2</sub> and *o*-H<sub>2</sub> to designate H<sub>2</sub> rotational levels  $j_2 = 0$  and  $j_2 = 1$ , respectively.

Scattering calculations were carried out at 198 and 190 energies from 1 to  $600\text{ cm}^{-1}$  for collisions of HCNO with *p*-H<sub>2</sub> and *o*-H<sub>2</sub>, respectively. At higher energies, vibrational excitation is energetically allowed, but these transitions are expected to have very small cross sections and can be ignored here. For total energies less than  $150\text{ cm}^{-1}$ , cross sections were calculated at  $1\text{ cm}^{-1}$  energy intervals, and progressively larger energy spacings were employed for higher energies. The calculations were checked for convergence with respect to the size of the HCNO rotational basis, the spacing of the radial grid, and the number of partial waves included in the computed integral cross section. For low total energies  $j_1^{\max}$  was set equal to 25; this limit was gradually increased to 45 at the highest total energies. The H<sub>2</sub> rotational basis included  $j_2 = 0$  and 2 for collisions with *p*-H<sub>2</sub> and only  $j_2 = 1$  for collisions with *o*-H<sub>2</sub>. The radial grid spacing was varied from 0.2 to  $0.03a_0$ .

Partial waves of total angular momentum  $J$  up to  $101\hbar$ , with all helicity values, were included in calculating integral cross sections. To show the convergence of the integral cross section with respect to the number of included partial waves, Fig. 4 displays the partial cross sections for HCNO–*o*-H<sub>2</sub> collisions for the strongest transitions at a total energy of  $100\text{ cm}^{-1}$ . It can be seen in Fig. 4 that the limit  $J_{\max} = 43$  captures the full magnitude of the integral cross sections for the total energy of  $100\text{ cm}^{-1}$ . The parameter  $J_{\max}$  was scaled as the square root of the total energy.

Exploratory calculations were carried out for *o*-H<sub>2</sub> collisions with inclusion of  $j_2 = 3$  in the H<sub>2</sub> rotation basis. Fig. 5 presents a comparison of calculated HCNO–H<sub>2</sub> cross sections for a total energy of  $100\text{ cm}^{-1}$  computed with H<sub>2</sub> rotational bases of  $j_2^{\max} = 1$  and 3. It can be seen that inclusion of  $j_2 = 3$  in the basis has a negligible effect on the magnitude of the cross sections. Indeed, it has become standard practice to include only  $j_2 = 1$  in the *o*-H<sub>2</sub> rotational basis.

Calculations for collisions at higher total energies involving both *p*-H<sub>2</sub> and *o*-H<sub>2</sub> would generate  $S$  matrices that would be too large for the program to determine integral cross sections. In such cases, the calculations were broken up to calculate partial cross sections for a subset of the partial waves. These were then added up to obtain the integral cross sections.

The computed state-to-state integral cross sections were employed to determine rate coefficients for collisions between HCNO rotational levels  $j_1 \leq 19$ , which have energies  $\leq 145\text{ cm}^{-1}$ , in collisions with *p*-H<sub>2</sub> and *o*-H<sub>2</sub>. The state-to-state rate coefficients were computed by averaging the energy-dependent state-to-state cross sections  $\sigma_{\text{f} \rightarrow \text{f}}$  over the collision energy  $E_c$ :

$$k_{\text{i} \rightarrow \text{f}} = \left( \frac{8}{\pi \mu (k_B T)^3} \right)^{1/2} \int_0^\infty \sigma_{\text{i} \rightarrow \text{f}}(E_c) E_c e^{-E_c/k_B T} dE_c \quad (5)$$

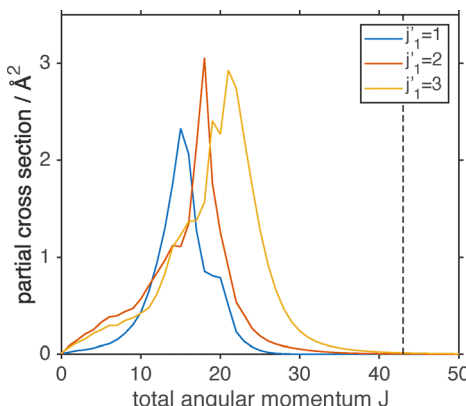


**Fig. 4** Partial cross sections for the collision of the  $j_1 = 0$  level of HCNO with  $o\text{-H}_2$  at a total energy of  $100 \text{ cm}^{-1}$ . The final levels are indicated in the legend. The vertical dashed line shows the highest partial wave included in the integral cross section.

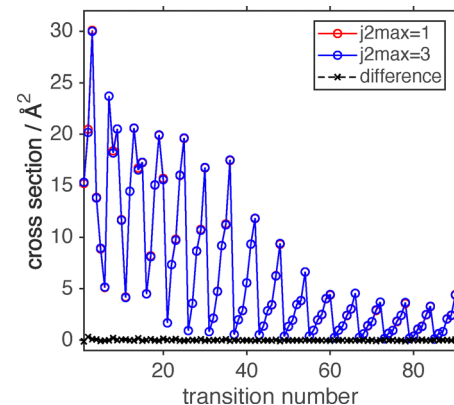


**Fig. 5** Comparison of integral cross sections for HCNO– $o\text{-H}_2$  collisions at a total energy of  $100 \text{ cm}^{-1}$ , computed with different  $o\text{-H}_2$  rotational bases.

where  $k_B$  is the Boltzmann constant and  $\mu$  is the collision reduced mass. The rate constants in eqn (5) were computed with the calculated cross sections up to the collision energy  $E_x$  corresponding to a total energy of  $600 \text{ cm}^{-1}$ . A high-energy tail for  $E_x \leq E_c \leq 2500 \text{ cm}^{-1}$ , obtained by using eqn (5) and assuming a constant cross section equal to the value at the highest computing energy, was added to obtain the final result for the rate constant. Rate coefficients were computed for the temperature range  $5\text{--}150 \text{ K}$  and rotational levels  $j_1 = 0$  to 20.

## 4 Results

In this section we investigate the magnitude and energy dependence of the state-to-state cross sections and rate coefficients. Fig. 6 presents plots of state-to-state integral cross sections for transitions in HCNO induced by collisions with  $p\text{-H}_2$  and  $o\text{-H}_2$  as a function of the collision energy. Panels (a) and (b) of Fig. 6 display cross sections for the excitation of the HCNO  $j_1 = 0$  rotational level to the  $j_1' = 1\text{--}5$  levels induced by collisions by  $p\text{-H}_2$  and  $o\text{-H}_2$ , respectively. As with all the calculated cross

sections, these cross sections rise sharply at the energetic threshold for each transition and then generally decrease in magnitude with increasing collision energy.

Some structure in the energy dependence of the cross sections at low collision energy for collisions of HCNO with  $p\text{-H}_2$  is observed in Fig. 6(a). This structure is caused by overlapping resonances due to formation and decay of quasi-bound levels built upon the potential well.<sup>50,51</sup> There are many more scattering levels correlating with the HCNO– $o\text{-H}_2$  asymptote because of the non-zero angular momentum of the hydrogen molecule in this case. Hence, the resonances in the case of  $o\text{-H}_2$  collisions strongly overlap, and no discernible structure is observed for collision of HCNO with  $o\text{-H}_2$ .

The  $j_1 = 0 \rightarrow j_1' = 2$  transition in collision with  $p\text{-H}_2$  is more than twice as large as the other  $j_1 = 0 \rightarrow j_1'$  transitions; the latter all have similar magnitudes. In the case of the collision of HCNO ( $j_1 = 0$ ) with  $o\text{-H}_2$ , the cross sections are considerably larger than the cross sections for the corresponding transitions involving collision with  $p\text{-H}_2$ . Here, the cross section with the greatest magnitude is for the  $j_1 = 0 \rightarrow j_1' = 3$  transition.

Panels (c) and (d) of Fig. 6 present cross sections for the de-excitation of the HCNO  $j_1 = 5$  rotational level caused by collisions with  $p\text{-H}_2$  and  $o\text{-H}_2$ , respectively. As with the excitation cross sections displayed in Fig. 6(a) and (b) the de-excitation cross sections rise sharply at their respective energy thresholds and then decrease with increasing collision energy. The cross sections are also seen to decrease with increasing change  $\Delta j_1$  in the rotational angular momentum. Finally, the de-excitation cross sections are seen to be significantly larger for collisions with  $o\text{-H}_2$  than with  $p\text{-H}_2$ . This behavior of the cross sections has been seen in the state-to-state collisions of

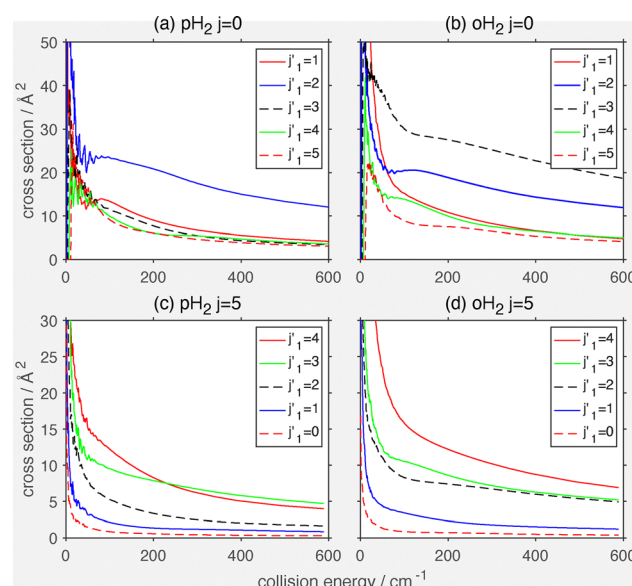


**Fig. 6** Integral cross sections as a function of the collision energy for the excitation of HCNO ( $j_1 = 0$ ) in collisions with (a)  $p\text{-H}_2$  and (b)  $o\text{-H}_2$ , respectively, and the de-excitation of HCNO ( $j_1 = 5$ ) in collisions with (a)  $p\text{-H}_2$  and (b)  $o\text{-H}_2$ , respectively. The final rotational levels  $j_1'$  are indicated in the legends.



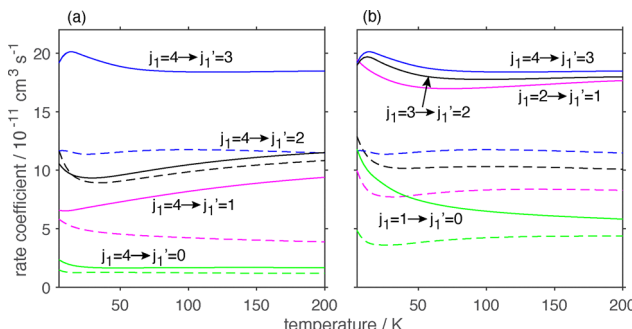


Fig. 7 Rate coefficients as a function of temperature for (a) the de-excitation of the  $j_1 = 4$  level induced by collisions with  $p\text{-H}_2$  and  $o\text{-H}_2$  and (b)  $\Delta j_1 = -1$  transitions from the  $j_1 = 1\text{--}4$  levels induced by collisions with  $p\text{-H}_2$  and  $o\text{-H}_2$ . Rate coefficients for collisions with  $p\text{-H}_2$  and  $o\text{-H}_2$  are indicated by dashed and solid lines, respectively.

many molecule– $\text{H}_2$  complexes.<sup>50–55</sup> The larger cross sections for collisions with  $o\text{-H}_2$  vs.  $p\text{-H}_2$  has been ascribed to the fact that the full anisotropy of the PES is experienced in collisions of the molecule with  $o\text{-H}_2$ .

Rate coefficients as a function of temperature are presented in Fig. 7. Panel (a) of Fig. 7 presents rate coefficients for the de-excitation of the HCNO  $j_1 = 4$  level to the  $j_1' = 0\text{--}3$  levels in collisions with  $p\text{-H}_2$  and  $o\text{-H}_2$ . As with the cross sections for these transitions plotted in panels (c) and (d) of Fig. 6 the rate coefficients involving collisions involving comparable transitions with  $o\text{-H}_2$  are generally significantly larger than the rate coefficients for collisions with  $p\text{-H}_2$ . In the case of the  $j_1 = 4 \rightarrow j_1' = 2$  and  $0$  transitions, the rate coefficients for collisions with  $o\text{-H}_2$  are only slightly larger than for collisions with  $p\text{-H}_2$ . We also see that the rate coefficients plotted in Fig. 7 are relatively independent of temperature.

Fig. 7(b) presents plots of the rate coefficients for  $\Delta j_1 = -1$  transitions from the HCNO  $j_1 = 1\text{--}4$  levels induced by collisions with  $p\text{-H}_2$  and  $o\text{-H}_2$ . For all the transitions, the rate coefficients involving collisions with  $o\text{-H}_2$  are significantly larger than those involving collisions with  $p\text{-H}_2$ . For collisions with both  $p\text{-H}_2$  and  $o\text{-H}_2$  the rate coefficient for the  $j_1 = 1 \rightarrow j_1' = 0$  transition has the smallest rate coefficient of the  $\Delta j_1 = -1$  transitions. The rate coefficients plotted in Fig. 7(b) for collisions with  $o\text{-H}_2$  are approximately independent of temperature. By contrast, the rate coefficients of these  $\Delta j_1 = -1$  transitions in HCNO involving collisions with  $p\text{-H}_2$  increase as a function of the temperature.

## 5 Discussion and conclusion

Calculation of rate coefficients using He as a surrogate for  $\text{H}_2$  has been employed for a number of systems since treating collisions of He rather than  $\text{H}_2$  is much simpler. Approximate rate coefficients for  $\text{H}_2$  collisions are then obtained by scaling by the square root of the reduced collision masses [see eqn (5)].<sup>56,57</sup> As noted in the Introduction, Naindouba *et al.*<sup>25</sup> have computed rate coefficients describing transitions between

rotational levels of HCNO induced by collisions with He, using a HCNO–He PES that they computed.

Cernicharo *et al.*<sup>18</sup> have employed these HCNO–He rate coefficients, scaled to approximate HCNO– $\text{H}_2$  rate coefficients in a radiative transfer modeling of these observations of HCNO lines in TMC-1. With the availability of the HCNO– $\text{H}_2$  rate coefficients, the accuracy of scaling HCNO–He rate coefficients to describe HCNO– $\text{H}_2$  rate coefficients can be checked. Fig. 8 compares these rate coefficients obtained by these two approaches for the lowest four  $\Delta j_1 = -1$  transitions. We see that while the scaled HCNO–He rate coefficients are of the same rough magnitude as the HCNO– $\text{H}_2$  rate coefficients, the temperature dependence of the scaled HCNO–He rate coefficients significantly disagrees with the temperature dependence of the HCNO– $\text{H}_2$  rate coefficients. Walker *et al.*<sup>58</sup> have explored the validity of this approximation and conclude that it is not valid on physical and mathematical grounds.

As noted above, the goal of this work is to provide rate coefficients for transitions between HCNO rotational levels induced by collisions with  $\text{H}_2$  for use in radiative transfer calculations for analysis of HCNO astronomical observations. As an example of the utility of these data, we carry out a simple radiative transfer calculation. Marcelino *et al.*<sup>17</sup> estimated abundances of the HNCO and HCNO isomers in the starless cores that they observed. We consider the HCNO  $j = 4\text{--}j = 3$  line at 91.751 GHz and the HNCO  $4_{04}\text{--}3_{03}$  line at 87.925 GHz, which were used by Marcelino *et al.*<sup>17</sup> It should be noted that these authors did carry out non-LTE calculations using unpublished HNCO rate coefficients computed by S. Green (presumably with He as the collision partner) for both HNCO and HCNO lines.

We employ the RADEX code<sup>22</sup> here to perform some simple non-LTE calculations on the HCNO and HNCO lines listed above. The HCNO– $\text{H}_2$  rate coefficients computed in this work and the HNCO– $\text{H}_2$  rate coefficients calculated by Sahnoun *et al.*<sup>24</sup> were utilized in the RADEX calculations. We assume HCNO and HNCO column densities of  $3 \times 10^{12}$  and  $5 \times 10^{10}$   $\text{cm}^{-2}$ , respectively, a linewidth of  $1 \text{ cm}^{-1}$ , and a kinetic

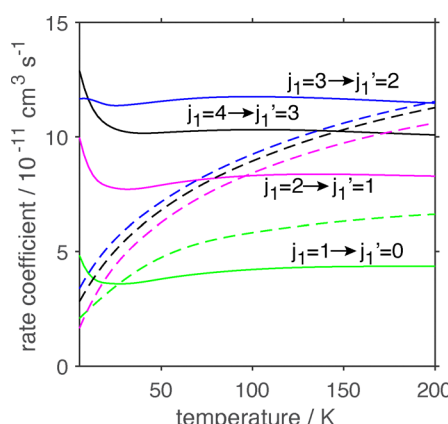
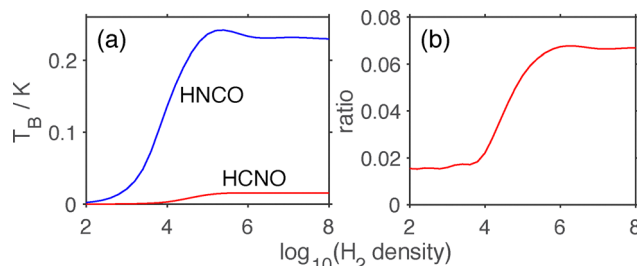


Fig. 8 Comparison of  $\Delta j_1 = -1$  HCNO– $\text{H}_2$  rate coefficients computed in this work (solid lines) with HCNO–He rate coefficients calculated by Naindouba *et al.*<sup>25</sup> (dashed lines) and scaled by the square root of the ratio of the HCNO– $\text{H}_2$  and HCNO–He collision reduced masses.



**Fig. 9** (a) The computed brightness temperature  $T_B$  of the HNCO  $4_{04}-3_{03}$  and HCNO  $j = 4-j = 3$  lines as a function of the  $H_2$  volume density. (b) Ratio of the computed HCNO and HNCO line intensities plotted in panel (a).

temperature of 10 K, consistent with the parameters used by Marcelino *et al.*<sup>17</sup> The cosmic microwave background was set to 2.73 K.

The left-hand panel of Fig. 9 displays the brightness temperatures  $T_B$  for the HCNO and HNCO lines as a function of the assumed  $H_2$  volume density. It can be seen that the intensities of both the HNCO and HCNO lines are small at the lowest assumed  $H_2$  volume density and increases as a function of the  $H_2$  density. The line intensities are then approximately constant for  $H_2$  densities above  $10^6 \text{ cm}^{-3}$ , and LTE is reached at the highest  $H_2$  densities. The right-hand panel of Fig. 9 presents the ratio of the computed HCNO and HNCO line intensities. It can be seen that the ratio varies strongly for  $H_2$  densities between  $10^4$  and  $10^6 \text{ cm}^{-3}$ . This range of  $H_2$  densities is commonly found for these astronomical objects. We conclude that the use of accurate rate coefficients in radiative transfer models is important in determining accurate abundances.

In this work, the potential energy surface describing the interaction of HCNO with  $H_2$  has been computed using explicitly correlated coupled cluster theory [CCSD(T)-f12a] and a correlation consistent aug-cc-pVTZ basis set. The dissociation energy  $D_e$  was determined to equal  $289.1 \text{ cm}^{-1}$ , and an equilibrium intermolecular separation of  $5.64a_0$  was found. Time independent quantum close coupling calculations were carried out with the aid of this PES to determine state-to-state integral cross sections for transfer between the HCNO rotational levels induced by collision with  $p\text{-H}_2$  and  $p\text{-H}_2$ . As mentioned below, tables of these rate coefficients will be made available in databases. The utility of these data will be radiative transfer calculations for accurate estimates of HCNO abundances, and also for providing information on the physical conditions of the interstellar medium.

## Author contributions

Paul J. Dagdigian: conceptualization; investigation; software; writing – original draft; writing – review and editing.

## Conflicts of interest

There are no conflicts to declare.

## Data availability

The computed rate coefficients for transitions between HCNO rotational levels induced by collisions with both  $p\text{-H}_2$  and  $o\text{-H}_2$  will be made available through the EMAA<sup>59</sup> and BASECOL<sup>60</sup> databases.

## Acknowledgements

The calculations reported in this work were performed at the Advanced Research Computing at Hopkins (ARCH) core facility (ARCH), which is supported by the National Science Foundation (NSF) under grant no. OAS-1920103.

## References

- 1 L. E. Snyder and D. Buhl, *Astrophys. J.*, 1972, **177**, 619.
- 2 B. E. Turner, *Astrophys. J. Suppl.*, 1991, **76**, 627–686.
- 3 K.-J. Kuan and L. E. Snyder, *Astrophys. J.*, 1996, **470**, 981–1000.
- 4 S. Martín, M. A. Requena-Torres, J. Martín-Pintado and R. Mauersberger, *Astrophys. J.*, 2008, **678**, 245–254.
- 5 G. A. Blake, E. Sutton, C. R. Masson and T. G. Phillips, *Astrophys. J.*, 1987, **315**, 621–645.
- 6 E. F. van Dishoeck, G. A. Blake, D. J. Jansen and T. D. Groesbeck, *Astrophys. J.*, 1995, **447**, 760–782.
- 7 G. H. Macdonald, A. G. Gibb, R. J. Habing and T. J. Millar, *Astron. Astrophys., Suppl. Ser.*, 1996, **119**, 333–367.
- 8 S. E. Bisschop, J. K. Jorgensen, T. L. Bourke, S. Bottinelli and E. F. van Dishoeck, *Astron. Astrophys.*, 2008, **488**, 959.
- 9 N. J. Rodríguez-Fernández, M. Tadalla, F. Gueth and R. Bachiller, *Astron. Astrophys.*, 2010, **516**, A98.
- 10 D. S. Meier and J. L. Turner, *Astrophys. J.*, 2005, **618**, 259–280.
- 11 D. Meier and J. L. Turner, *Astrophys. J.*, 2006, **618**, 259–280.
- 12 S. Martín, J. Martín-Pintado and R. Mauersberger, *Astrophys. J.*, 2009, **694**, 610–617.
- 13 J. Crovisier, *Faraday Discuss.*, 1998, **109**, 437–452.
- 14 N. Biver, D. Bockelée-Morvan, J. Crovisier, D. C. Lis, R. Moreno, P. Colom, F. Herpin, G. Paubert and M. Womack, *Astron. Astrophys.*, 2006, **449**, 1255–U240.
- 15 S. Brünken, C. A. Gottlieb, M. C. McCarthy and P. Thaddeus, *Astrophys. J.*, 2009, **697**, 880–995.
- 16 S. Brünken, A. Belloche, S. Martin, L. Verheyen and K. M. Menten, *Astron. Astrophys.*, 2010, **516**, A109.
- 17 N. Marcelino, J. Cernicharo, B. Tercero and E. Roueff, *Astrophys. J.*, 2009, **690**, L27–L30.
- 18 J. Cernicharo, M. Agúndez, C. Cabezas, B. Tercero, R. Fuentetaja, N. Marcelino and P. de Vicente, *Astron. Astrophys.*, 2024, **682**, L4.
- 19 H. K. Bodenseh and M. Winnewisser, *Z. Naturforsch., A: Phys. Sci.*, 1969, **24**, 1973.
- 20 N. Marcelino, S. Brünken, J. Cernicharo, D. Quan, E. Roueff, E. Herbst and P. Thaddeus, *Astron. Astrophys.*, 2010, **516**, A105.



21 M. Mladenović, M. Lewerenz, M. C. McCarthy and P. Thaddeus, *J. Chem. Phys.*, 2009, **131**, 174308.

22 F. F. S. van der Tak, J. H. Black, F. L. Schöier, D. J. Jansen and E. F. van Dishoeck, *Astron. Astrophys.*, 2007, **468**, 627–635.

23 C. P. Endres, S. Schlemmer, P. Schilke, J. Stutzki and H. S. P. Müller, *J. Mol. Spectrosc.*, 2016, **327**, 95–104.

24 E. Sahnoun, L. Wiesenfeld, K. Hammami and N. Jaidane, *J. Phys. Chem. A*, 2018, **122**, 3004–3012.

25 A. Naindouba, C. Nkema, Y. Ajili, K. Hammami, N. Gotoum and L. O. Owono, *Chem. Phys. Lett.*, 2015, **636**, 67–71.

26 M. Naouai and A. Jrad, *Mon. Not. R. Astron. Soc.*, 2022, **512**, 1177–1184.

27 K. Naskar, S. Ghosh and S. Adhikari, *J. Phys. Chem. A*, 2022, **126**, 3311–3328.

28 S. Hazra, K. Naskar, S. Adhikari and A. J. C. Varandas, *J. Phys. Chem. A*, 2024, **128**, 8833–8844.

29 B. Mandal, J. F. E. Croft, P. G. Jambrina, H. Guo, F. J. Aoiz and N. Balakrishnan, *Phys. Chem. Chem. Phys.*, 2024, **26**, 18368.

30 B. Mandal, J. F. E. Croft, P. J. Jambrina, H. Guo, F. J. Aoiz and N. Balakrishnan, *J. Phys. Chem. Lett.*, 2023, **14**, 817–824.

31 J. Loreau, F. Lique and A. Faure, *Astrophys. J. Lett.*, 2018, **853**, L5.

32 J. H. Teles, G. Maier, B. A. Hess, L. J. Schaad, M. Winnewisser and B. P. Winnewisser, *Chem. Ber.*, 1989, **122**, 753–766.

33 P. R. Bunker, B. M. Landsberg and B. P. Winnewisser, *J. Mol. Spectrosc.*, 1979, **74**, 9–25.

34 H.-J. Werner, P. J. Knowles, F. R. Manby, J. A. Black, K. Doll, A. Hesselmann, D. Kats, A. Köhn, T. Korona, D. A. Kreplin, Q. Ma, T. F. Miller, A. Mitrushchenkov, K. A. Peterson, I. Polyak, G. Rauhut and M. Sibaev, *J. Chem. Phys.*, 2020, **152**, 144107.

35 T. B. Adler, G. Knizia and H.-J. Werner, *J. Chem. Phys.*, 2007, **127**, 221106.

36 T. H. Dunning, *J. Chem. Phys.*, 1989, **90**, 1007–1023.

37 D. E. Woon and T. H. Dunning, *J. Chem. Phys.*, 1993, **98**, 1358–1371.

38 F. Weigend, *Phys. Chem. Chem. Phys.*, 2002, **4**, 4285–4291.

39 F. Weigend, A. Köhn and C. Hättig, *J. Chem. Phys.*, 2002, **116**, 3175–3183.

40 F. B. van Duijneveldt, J. G. C. M. van Duijneveldt-van de Rijdt and J. H. van Lenthe, *Chem. Rev.*, 1994, **94**, 1873–1885.

41 C. Rist and A. Faure, *J. Math. Chem.*, 2012, **50**, 588–601.

42 S. Green, *J. Chem. Phys.*, 1975, **62**, 2271–2277.

43 R. N. Zare, *Angular Momentum*, Wiley, New York, 1988.

44 C. Rist, M. H. Alexander and P. Valiron, *J. Chem. Phys.*, 1993, **98**, 4662.

45 P. E. S. Wormer, J. A. K. G. C. Groenenboom and A. van der Avoird, *J. Chem. Phys.*, 2005, **122**, 244325.

46 P. J. Dagdigian, *J. Chem. Phys.*, 2023, **159**, 114302.

47 P. J. Dagdigian, *J. Chem. Phys.*, 2024, **535**, 247–253.

48 P. J. Dagdigian, *J. Chem. Phys.*, 2025, **162**, 174308.

49 M. H. Alexander, P. J. Dagdigian, H.-J. Werner, J. Kłos, B. Desrousseaux, G. Raffy and F. Lique, *Comput. Phys. Commun.*, 2023, **289**, 108761.

50 P. J. Dagdigian, *J. Chem. Phys.*, 2018, **148**, 024304.

51 P. J. Dagdigian, *J. Chem. Phys.*, 2020, **152**, 224304.

52 Y. Kalugina, J. Kłos and F. Lique, *J. Chem. Phys.*, 2013, **139**, 074301.

53 M. Hernández-Vera, Y. Kalugina, O. Denis-Alpizar, T. Stoecklin and F. Lique, *J. Chem. Phys.*, 2014, **140**, 224302.

54 H. C. Schewe, Q. Ma, N. Vanhaecke, X. Wang, J. Kłos, M. H. Alexander, S. Y. T. van de Meerakker, G. Meijer, A. van der Avoird and P. J. Dagdigian, *J. Chem. Phys.*, 2015, **142**, 204310.

55 Q. Ma, A. van der Avoird, J. Loreau, M. H. Alexander, S. Y. T. van de Meerakker and P. J. Dagdigian, *J. Chem. Phys.*, 2015, **143**, 044312.

56 F. Lique, R. Toboła, J. Kłos, N. Feautrier, A. Spielfiedel, L. F. M. Vincent, G. Chałasiński and M. H. Alexander, *Astron. Astrophys.*, 2008, **478**, 567–574.

57 J. Cernicharo, A. Spielfiedel, C. Balança, F. Dayou, M.-L. Senent, N. Feautrier, A. Faure, L. Cressiot-Vincent, L. Wiesenfeld and J. R. Pardo, *Astron. Astrophys.*, 2011, **531**, 103.

58 K. M. Walker, B. H. Yang, P. C. Stancil, N. Balakrishnan and R. C. Forrey, *Astrophys. J.*, 2014, **790**, 96.

59 A. Faure, A. Bacmann and R. Jacquot, *Astron. Astrophys.*, 2025, **700**, A266.

60 M. L. Dubernet, C. Boursier, O. Denis-Alpizar, Y. A. Ba, N. Moreau, C. M. Zwölf, M. A. Amor, D. Babikov, N. Balakrishnan, C. Balança, M. Ben Khalifa, A. Bergeat, C. T. Bop, L. Cabrera-González, C. Cárdenas, A. Chefai, P. J. Dagdigian, F. Dayou, S. Demes, B. Desrousseaux, F. Dumouchel, A. Faure, R. C. Forrey, J. Franz, R. M. García-Vázquez, F. Gianturco, A. Godard Palluet, L. González-Sánchez, G. C. Groenenboom, P. Halvick, K. Hammami, F. Khadri, Y. Kalugina, I. Kleiner, J. Kłos, F. Lique, J. Loreau, B. Mandal, B. Mant, S. Marinakis, D. Ndaw, P. Pirlot Jankowiak, T. Price, E. Quintas-Sánchez, R. Ramachandran, E. Sahnoun, C. Santander, P. C. Stancil, T. Stoecklin, J. Tennyson, F. Tonolo, R. Urzúa-Leiva, B. Yang, E. Yurtsever and M. Zóltowski, *Astron. Astrophys.*, 2024, **683**, A40.

